Rotational alignment effects in NO(X) + Ar inelastic collisions: An experimental study

M. Brouard,[1, a)] H. Chadwick,[1] C.J. Eyles,[1, b)] B. Hornung,[1] B. Nichols,[1] F.J. Aoiz,[2] P.G. Jambrina,[2] and S. Stolte[3]

[1)] *The Department of Chemistry, University of Oxford, The Physical and Theoretical Chemistry Laboratory, South Parks Road, Oxford, OX1 3QZ, United Kingdom.*

[2)] *Departamento de Química Física, Facultad de Química, Universidad Complutense, 28040 Madrid, Spain*

[3)] *Atomic and Molecular Physics Institute, Jilin University, Changchun 130012, China*[c)]

(Dated: 3 January 2013)

Rotational angular momentum alignment effects in the rotationally inelastic collisions of NO(X) with Ar have been investigated at a collision energy of 66 meV by means of hexapole electric field initial state selection coupled with velocity-map ion imaging final state detection. The fully quantum state resolved second order renormalized polarization dependent differential cross sections determined experimentally are reported for a selection of spin-orbit conserving and changing transitions for the first time. The results are compared with the findings of previous theoretical investigations, and in particular with the results of exact quantum mechanical scattering calculations. The agreement between experiment and theory is generally found to be good throughout the entire scattering angle range. The results reveal that the hard shell nature of the interaction potential is predominantly responsible for the rotational alignment of the NO(X) upon collision with Ar.

[a)]Electronic mail: mark.brouard@chem.ox.ac.uk

[b)]Current address: Institut fur Chemie und Biochemie, Freie Universitat Berlin, Takustr. 3 14195 Berlin, Germany.

[c)]Alternative affiliations: Laser Center, Vrije Universiteit, Amsterdam, De Boelelaan 1083, 1081 HV Amsterdam, The Netherlands and Laboratoire Francis Perrin, Bâtiment 522, DRECEM/SPAM/CEA Saclay, 91191 Gif sur Yvette, France

I.   INTRODUCTION

The experimental investigation of vector correlations in bimolecular scattering events provides detailed dynamical information.[1,2] The correlation between the initial and final relative velocities is quantified by the differential cross section (DCS), whilst the triple vector correlation between the initial and final relative velocities, $\boldsymbol{k}$ and $\boldsymbol{k'}$, and the final rotational angular momentum, $\boldsymbol{j'}$, is characterized by the polarization dependent differential cross section (PDDCS).[3–5] In the following work, combined with the theoretical study presented in the accompanying paper,[6] we aim to illustrate how measurements of the fully quantum state resolved renormalized PDDCSs, defined here by the notation $\rho_{q\pm}^{\{k\}}(\theta)$ for rank k and order q,[5,6] provide valuable information about the dynamics of molecular collisions.

Inelastic scattering of NO(X) by the rare gases has emerged as a prototype for studying interactions of open shell radicals with closed shell atoms. The unpaired electron in a π orbital gives rise to two spin-orbit levels, both of which can be populated as the result of a collision, leading to a breakdown in the Born-Oppenheimer approximation. Despite this complexity, these collisions are still amenable to exact quantum mechanical scattering calculations. Therefore, there have been many previous studies comparing experimental and theoretical rotational energy transfer[7–18] and differential cross-sections.[7,19–33]

The open shell nature of the NO(X) molecule also introduces the concept of parity conserving and parity changing transitions, depending on the initially populated Λ-doublet level, and that populated after the collision. Most of the studies mentioned above were performed with full Λ-doublet resolution of the final NO(X) quantum state, but without this level of resolution of the initial state. Recently, hexapole focussing has been used to select a unique Λ-doublet level of the NO(X) before the collision, and both the integral[9,10] and DCSs[20,23,24] have been measured for the inelastic scattering of NO(X) with helium and argon. The structure of the observed DCSs was shown to have a significant dependence on whether the parity of the NO(X) wavefunction was conserved or changed as a result of the collision,[20–25] highlighting the additional information gained from performing fully quantum state resolved studies. For NO(X)-Ar, multiple oscillations were observed for parity conserving transitions, but only a single peak for parity changing transitions. These observations were rationalized in terms of the semiclassical framework described by Schinke,[34] and could be attributed to interference effects between trajectories which sampled different parts of

1

the NO(X) molecule. The experimental DCSs were also shown to be in excellent agreement with those obtained from quantum mechanical calculations.[23,24] As the experimental measurement of the DCSs provides a sensitive probe of the underlying potential energy surfaces (PESs), the agreement validates both the PESs employed[8] and the theoretical methods used.

The study of polarization effects in the inelastic scattering of NO(X) with the rare gases has received considerably less attention. The collision induced alignment for NO(X) with He has been measured by Meyer,[35] and with Ne by Kim *et al.*.[36,37] In both cases, the alignment parameters that could be extracted experimentally were shown to be in good agreement with those from theoretical quantum mechanical calculations, and those predicted by the (classical) kinematic apse model (see further below).[38–40] The collision induced polarization of NO(X) with argon, as considered here, has also been the subject of previous experimental studies, with both orientation[41,42] and alignment[43,44] being measured. The trends in the alignment parameters from these studies qualitatively followed those obtained theoretically, but the quantum mechanical calculations appeared to overestimate the magnitude of the alignment. This was attributed to inaccuracies in the short range region of the PESs of Alexander.[8] The same PESs have subsequently been used to calculate the fully Λ-doublet state resolved DCSs, which as mentioned above are in excellent agreement with those obtained experimentally.[23,24]

In the current paper we present new experimental results on the collision induced rotational angular momentum alignment for the inelastic scattering of NO(X) by Ar. For the first time, the alignment data are presented with full quantum state resolution for both the initial and the final state of the NO(X). The results are compared in detail with the theoretical predictions presented in the accompanying paper.[6] The experimental data provide a further test of the non-adiabatic quantum mechanical calculations, and of the PESs which they employ. The accompanying paper considers in detail the applicability of a quantum mechanical variant of the kinematic apse model to the NO(X) + Ar system.[6] We return to a discussion of the applicability of this model to the inelastic scattering of NO(X) by Ar in the discussion and conclusions of the present paper.

The paper is organized as follows. Firstly, in section II the experimental procedures employed are described. This section also includes a brief description of the quantum mechanical (QM) scattering calculations used to simulate the experimental results, with special emphasis on the determination of the polarization moments. In section III, the formulae

used to determine the rotational angular momentum polarization are summarized. The data analysis method used to extract the polarization parameters from the experimental images is also introduced. The experimental results are presented and discussed in section IV. Section V provides a short conclusion of the main findings of the paper. Finally, for completeness an overview of the different approaches treating the effect of the rotational polarization on the signal intensity for one photon transitions is provided in the Supplementary Material.[45]

II. METHODS

The experiments employed a hexapole electric field to select the initial state of the NO(X), and (1+1') resonantly enhanced multiphoton ionization (REMPI) coupled with velocity-map ion imaging to detect the final state.[20,23,24,46,47] 16% nitric oxide (BOC) was seeded in Ar at a pressure of 3 bar, and the molecular beam was produced using a General valve pulsed at a repetition rate of 10 Hz.[23,24] The skimmed NO(X) beam entered into the hexapole electric field where the molecules having $|\Omega, j, \epsilon\rangle = |1/2, 0.5, -1\rangle$ were state selected. The proportion of the molecules in the beam in this particular state after leaving the hexapole was better than 99%.[20] The molecules then passed through a field free region so that the beam converged in the center of the scattering chamber, where the mean NO(X) velocity was determined to be $625\,\mathrm{m\,s^{-1}}$.[23,24] The argon beam was also produced using a General valve, but was pulsed on for two shots then off for two shots of the NO beam to allow the background noise to be recorded simultaneously, minimizing any errors associated with experimental fluctuations. The beam was passed through a 2 mm diameter skimmer before intersecting the NO(X) beam at the center of the scattering chamber. The velocity of the argon beam was determined to be $590\,\mathrm{m\,s^{-1}}$, giving rise to a center-of-mass collision energy, $E_{\mathrm{coll}} = 66\,\mathrm{meV}$.[23,24]

The $\lambda = 308\,\mathrm{nm}$ output of a Lambda Physik XeCl excimer laser operating synchronously at 10 Hz was passed through a beam splitter. About 90% of the beam pumped a tunable Lambda Physik dye laser, operating around 452 nm, the output of which was frequency doubled to wavelengths in the region of 226 nm, and tuned to the NO (A ← X) transition of interest. The probe radiation was passed through a Rochon polarizer and photo-elastic modulator before entering the scattering chamber. For the specific experiments described here, the final states $|1/2, 6.5, -1\rangle$, $|1/2, 7.5, +1\rangle$, $|1/2, 7.5, -1\rangle$, $|1/2, 8.5, -1\rangle$,

3

$|1/2, 10.5, -1\rangle$, $|3/2, 5.5, +1\rangle$, and $|3/2, 9.5, +1\rangle$ were chosen to be recorded. For the spin-orbit conserving collisions, the R_{21} REMPI branch was used to probe the $\epsilon' = -1$ (f) states, and the $Q_{21}+R_{11}$ mixed branch was used for the $\epsilon' = +1$ (e) states. For the spin-orbit changing transitions the $Q_{22}+R_{12}$ mixed branch was used. The experimental arrangement is such that the laser propagation axis, $\boldsymbol{k}_{\mathrm{p}}$, lies in the plane defined by the molecular beams and was almost perpendicular to the initial relative velocity, $\boldsymbol{k}$, of the collision partners (see the left panel of Fig. 1). The photo-elastic modulator was used to switch the polarization of the dye laser beam on every pulse of the NO beam between horizontal (H) and vertical (V) linear polarization with respect to the plane containing the molecular beams, such that to a good approximation the polarization vector was either parallel to the relative velocity or perpendicular to it, out of the scattering plane.

The remaining 10% of the 308 nm laser beam was used to ionize the NO(A) radicals, which allowed the dye laser power to be kept low to avoid saturating the transition.[48] The images reported here were recorded with at least 95% $(1+1')$ REMPI signal. The laser entered the chamber perpendicular to the pump laser, again in the plane defined by the molecular beams. The ions formed from the NO(A) molecules were detected using velocity mapped ion imaging, and the signal recorded with a CCD camera. On average, 200,000 laser shots were used for each transition with both the H and V images recorded simultaneously. The raw images were background subtracted, and the normalized difference images, $(V-H)/(V+H)$, were subsequently determined. To avoid excessive noise in the outer regions of $(V-H)/(V+H)$ images, a threshold was applied by setting them to zero when the summed $(V+H)$ image intensity was less than a few percent of the maximum. This procedure was adopted for both the experimental and the simulated data, described in section III B 2.

The experimental results are compared with those obtained from full non-adiabatic close-coupled QM scattering calculations. These were carried out, as described in the accompanying paper,[6] using the HIBRIDON[49–51] program suite on the V_{sum} and V_{diff} CCSD(T) PESs of Alexander.[8] The resulting orbital angular momentum representation scattering matrices were transformed to the helicity representation using the standard transformation formula.[52]

Once the helicity-representation scattering matrices were calculated, the vector properties of the collision (*i.e.* the differential cross sections, differential reagent polarization moments, and differential product polarization moments) were determined using the methods described in refs. 5 and 53.

III. DATA ANALYSIS

A. Signal intensity and polarization parameters

The data analysis performed here is based on the formalism developed by Fano and Macek.[54] However, this treatment is equivalent to others commonly employed in the literature, as discussed in detail in the Supplementary Material.[45] Fano and Macek developed a formula for the intensity of the $j_i \rightarrow j_f$ one-photon transition in a rotationally polarized medium in their seminal paper in 1973.[54] Their expression was originally formulated in terms of polarization parameters, expressed here in the detector frame,

$$I = CS \left[1 + \tfrac{3}{2} h^{(1)}(j_i, j_f) A_0^{\{1\}\text{det}} \sin(2\beta) / \sqrt{j_i(j_i+1)} \right.$$
$$\left. - \tfrac{1}{2} h^{(2)}(j_i, j_f) A_0^{\{2\}\text{det}} + \tfrac{\sqrt{3}}{2} h^{(2)}(j_i, j_f) A_{2+}^{\{2\}\text{det}} \cos(2\beta) \right], \tag{1}$$

where C is a constant, S is a line strength, and $h^{(k)}(j_i, j_f)$ is a line strength factor for the polarization moment of order k, and is defined[54]

$$h^{(k)}(j_i, j_f) = (-1)^{j_i - j_f} \left\{ \begin{matrix} j_i & j_i & k \\ 1 & 1 & j_f \end{matrix} \right\} \Big/ \left\{ \begin{matrix} j_i & j_i & k \\ 1 & 1 & j_i \end{matrix} \right\}. \tag{2}$$

In terms of the Fano and Macek moments defined in Eqs. (11)-(13) of Ref. 54, the polarization parameters $A_0^{\{2\}\text{det}} \equiv A_0^{\text{det}}$ and $A_{2+}^{\{2\}\text{det}} \equiv A_{2+}^{\text{det}} \times \sqrt{3}$, and $A_0^{\{1\}\text{det}} \equiv O_0^{\text{det}} \times \sqrt{j_i(j_i+1)}$, respectively. Therefore, the coefficient in front of the parameter $A_{2+}^{\{2\}\text{det}}$ in the above expressions differs by a factor of $1/\sqrt{3}$ from that originally given by Fano and Macek, due to the non-standard normalization they used for their alignment parameters.[55] The superscript 'det' employed here emphasizes that these moments refer to the so-called detector (or laser) frame in which the alignment parameters are defined. In the Fano and Macek treatment, the principal axis of the detector frame, $\boldsymbol{\zeta}$, is parallel to the laser propagation axis, $\boldsymbol{k}_{\text{p}}$ (see the middle panel of Fig. 1). The polarization vector, $\hat{\boldsymbol{\epsilon}}$, is defined in the detector frame so that $\hat{\boldsymbol{\epsilon}} = (\cos\beta, i\sin\beta, 0)$, where its major component is always parallel with the first axis, $\hat{\boldsymbol{\xi}}$, of the detector frame, whereas the second axis, $\hat{\boldsymbol{\eta}}$, is chosen such that the frame is right handed. In the case of linearly polarized light, $\beta = 0$, and thus $\hat{\boldsymbol{\epsilon}} = (1, 0, 0)$. In the case of right or left circularly polarized light $\beta = \pm\frac{\pi}{4}$, thus $\hat{\boldsymbol{\epsilon}} = \frac{1}{\sqrt{2}}(1, \pm i, 0)$.

The primary frame used in this study is the scattering frame, defined in Fig. 1. However, the intensity expression above is given in terms of detector frame polarization moments, and

therefore the latter have to be expressed using the scattering frame polarization moments. This can be achieved by rotation of the scattering frame quantities *via* the three Euler angles, $\Gamma_{V/H} = (\chi, \Theta, \varphi)$, which describe the relative orientation of the two frames. Θ is the polar angle of the laser propagation axis, $\boldsymbol{\zeta} = \boldsymbol{k}_p$, with respect to the initial relative velocity; φ is the azimuth of the laser propagation axis in the scattering frame. Finally, χ is the third angle which is needed to specify the relative orientation of the two frames. The angles Θ, and φ are shown in the right panel of Fig. 1. Θ and φ are independent of the polarization, whilst χ depends on the polarization of the light employed. The rotation formulae were provided by Fano and Macek,[54] and are given by the equations

$$A_0^{\{1\}det} = A_{1-}^{\{1\}} \sin\Theta \sin\varphi$$
$$A_0^{\{2\}det} = A_0^{\{2\}} \tfrac{1}{2} \left(3\cos^2\Theta - 1\right) + A_{1+}^{\{2\}} \tfrac{\sqrt{3}}{2} \sin 2\Theta \cos\varphi + A_{2+}^{\{2\}} \tfrac{\sqrt{3}}{2} \sin^2\Theta \cos 2\varphi$$
$$A_{2+}^{\{2\}det} = A_0^{\{2\}} \tfrac{\sqrt{3}}{2} \sin^2\Theta \cos 2\chi \tag{3}$$
$$+ A_{1+}^{\{2\}} \left[\sin\Theta \cos\varphi \sin 2\chi + \sin\Theta \cos\Theta \sin\varphi \cos 2\chi\right]$$
$$+ A_{2+}^{\{2\}} \left[\tfrac{1}{2}\left(1 + \cos^2\Theta\right)\cos 2\varphi \cos 2\chi - \cos\Theta \sin 2\varphi \sin 2\chi\right] ,$$

where we have employed the Hertel-Stoll[56] normalized alignment parameters, as indicated in Table I. As with Eq. (1), note that the coefficients in front of the $A_{1+}^{\{2\}}$ and $A_{2+}^{\{2\}}$ parameters differ from those given in Fano and Macek,[54] because of the unconventional normalization that they employed.

Eqs. (3) can be recast in terms of either the renormalized PDDCSs or the alignment parameters used in the present work.[5,6] With the aid of Table I, and using the renormalized PDDCSs, $\rho_{q\pm}^{\{k\}}(\theta)$, we may write

$$A_0^{\{1\}det} = c_1(j_i)\rho_{1-}^{\{1\}}(\theta) \sin\Theta \sin\varphi$$
$$A_0^{\{2\}det} = c_2(j_i)\left\{\rho_0^{\{2\}}(\theta)\tfrac{1}{2}\left(3\cos^2\Theta - 1\right) + \rho_{1+}^{\{2\}}(\theta)\tfrac{\sqrt{3}}{2}\sin 2\Theta \cos\varphi + \rho_{2+}^{\{2\}}(\theta)\tfrac{\sqrt{3}}{2}\sin^2\Theta \cos 2\varphi\right\}$$
$$A_{2+}^{\{2\}det} = c_2(j_i)\left\{\rho_0^{\{2\}}(\theta)\tfrac{\sqrt{3}}{2}\sin^2\Theta \cos 2\chi \right. \tag{4}$$
$$+ \rho_{1+}^{\{2\}}(\theta)\left[\sin\Theta \cos\varphi \sin 2\chi + \sin\Theta \cos\Theta \sin\varphi \cos 2\chi\right]$$
$$\left. + \rho_{2+}^{\{2\}}(\theta)\left[\tfrac{1}{2}\left(1 + \cos^2\Theta\right)\cos 2\varphi \cos 2\chi - \cos\Theta \sin 2\varphi \sin 2\chi\right]\right\} ,$$

where θ is the center-of-mass scattering angle. The $c_k(j_i)$ factors appearing in these expressions are required to transform those of Eq. (3), in terms of alignment parameters, into ones in terms of renormalized PDDCSs within the Hertel-Stoll normalization, $\rho_{q\pm}^{\{k\}}(\theta)$. The appropriate scaling factors are $c_1(j_i) = [j_i(j_i+1)]^{-1/2}$ and $c_2(j_i) = [(2j_i+3)(2j_i-1)/(j_i(j_i+1))]^{1/2}$.

[3,5] Once the expression for the intensity, Eq. (1), is integrated over scattering angle, θ, identical expressions hold to those of Eq. (4) for the alignment parameters, $a_{q\pm}^{\{k\}}$.

The intensity differences between the images acquired using horizontally or vertically polarized light stem from the different values of $\Gamma_{V/H} = (\chi_{V/H}, \Theta, \varphi)$ linked to alternative linear polarizations of the laser light. Specifically, for horizontal polarization of the light, when the electric vector lies in the plane of the two molecular beams, we have to a good approximation $\Gamma_H = (\pi, \pi/2, \varphi)$, whereas for vertically polarized light $\Gamma_V = (\pi/2, \pi/2, \varphi)$. Chandler and coworkers used simplified versions of the above equations to retrieve the experimental renormalized PDDCSs, assuming an idealized in-plane experimental geometry, in which $\varphi = 0$.[44] In the present work, no such simplifications are introduced since every scattering event is considered regardless of whether or not it is in-plane or out-of-plane.

B. Method of data fitting

The experimentally derived renormalized PDDCSs were obtained using a Fourier moment fitting method.[23–25,57] The Fourier moments of an appropriate basis set were fitted against those of the experimental normalized difference image, $(V−H)/(V+H)$. In the following subsection we describe the simulation of the basis functions, the fitting method, and the error analysis performed.

1. Basis sets

The detection probability, $\imath_{V/H}(x_n, y_n)$, of a single scattering event with either vertical or horizontal polarization, n, can be written as a product of three terms

$$\imath_{V/H}(x_n, y_n) = z(x_n, y_n) \, P_{\text{scat}}(\theta_n) \, P_{V/H}(\theta_n; \Gamma_{V/H}^n) \,, \tag{5}$$

where $z(x_n, y_n)$ is the apparatus function for a pixel with coordinates (x_n, y_n) on the detector, $P_{\text{scat}}(\theta_n)$ is the angular scattering distribution (proportional to the DCS), and $P_{V/H}(\theta_n; \Gamma_{V/H}^n)$ is the polarization dependent transition probability. The Euler angles, $\Gamma_{V/H}^n$, were determined from the relative orientation of the laser and collision frame and used to calculate $P_{V/H}(\theta_n; \Gamma_{V/H}^n)$ for a given scattering event. In the following, we discuss how a basis set image was constructed using a batch of 2×10^8 individual trajectories. For each trajectory,

the initial velocities and the spatial and temporal coordinates were sampled as described in detail elsewhere,[24] and summarized below in section III B 2.

The polarization dependent transition probability, $P_{\mathrm{V/H}}(\theta_n; \Gamma^n_{\mathrm{V/H}})$, referred to in Eq. (5), can be written in terms of the renormalized PDDCSs, $\rho^{\{k\}}_{q\pm}(\theta_n)$,[6] as

$$P_{\mathrm{V/H}}(\theta_n; \Gamma^n_{\mathrm{V/H}}) = CS \left[1 + \sum_{kq} \rho^{\{k\}}_{q\pm}(\theta_n) F^{\{k\}}_{q\pm}(\Gamma^n_{\mathrm{V/H}}) \right] . \tag{6}$$

The $F^{\{k\}}_{q\pm}(\Gamma^n_{\mathrm{V/H}})$ functions contain all the geometrical information needed to calculate the contribution of a certain $\rho^{\{k\}}_{q\pm}(\theta_n)$. In the case of alignment measurements, three $k = 2$ functions for $q = 0$, 1, and 2 contribute to the signal, and, combining Eqs. (1) and (4), are given explicitly as

$$F^{\{2\}}_0(\Gamma^n_{\mathrm{V/H}}) = \tfrac{1}{4} h^{(2)}(j_i, j_f) c_2(j_i) \left(3 \sin^2 \Theta_n \cos 2\chi - \left[3 \cos^2 \Theta_n - 1 \right] \right) \tag{7}$$

$$F^{\{2\}}_{1+}(\Gamma^n_{\mathrm{V/H}}) = \tfrac{\sqrt{3}}{4} h^{(2)}(j_i, j_f) c_2(j_i) \left(2 \sin \Theta_n \cos \varphi_n \sin 2\chi \right.$$
$$\left. + 2 \sin \Theta_n \cos \Theta_n \sin \varphi_n \cos 2\chi - \sin 2\Theta_n \cos \varphi_n \right)$$

$$F^{\{2\}}_{2+}(\Gamma^n_{\mathrm{V/H}}) = \tfrac{\sqrt{3}}{4} h^{(2)}(j_i, j_f) c_2(j_i) \left(\left[1 + \cos^2 \Theta_n \right] \cos 2\varphi_n \cos 2\chi \right.$$
$$\left. - 2 \cos \Theta_n \sin 2\varphi_n \sin 2\chi - \sin^2 \Theta_n \cos 2\varphi_n \right) .$$

Their values depend on whether the probe light is horizontally or vertically polarized, but are independent of the scattering angle, and of the apparatus function.

Let us write the renormalized PDDCSs for even n in terms of a series expansion

$$\rho^{\{k\}}_{q\pm}(\theta_n) = \sum_{l=0}^{N^{\{k\}}_{q\pm}} c^{\{k\}}_{q\pm,l} \, a_l \, W_l(\theta_n) , \tag{8}$$

where $W_l(\theta_n)$ constitute a suitable, orthogonal set of functions (e.g., Legendre polynomials), $c^{\{k\}}_{q\pm,l}$ are the expansion coefficients, and a_l are a set of known l-dependent normalization coefficients. Substituting Eq. (8) into Eq. (6) and then into Eq. (5) yields the key expression below for the intensity corresponding to a single scattering event

$$\imath_{\mathrm{V/H}}(x_n, y_n) = CS \left[P_{\mathrm{scat}}(\theta_n) z(x_n, y_n) + \sum_{k,q} \sum_{l=0}^{N^{\{k\}}_{q\pm}} c^{\{k\}}_{q\pm,l} g^{\{k\}}_{q\pm,l}(x_n, y_n, \theta_n; \Gamma^n_{\mathrm{V/H}}) \right] , \tag{9}$$

where

$$g^{\{k\}}_{q\pm,l}(x_n, y_n, \theta_n; \Gamma^n_{\mathrm{V/H}}) = a_l \, W_l(\theta_n) \, F^{\{k\}}_{q\pm}(\Gamma^n_{\mathrm{V/H}}) \, z(x_n, y_n) \, P_{\mathrm{scat}}(\theta_n) . \tag{10}$$

8

Note that the evaluation of the first term in Eq. (9) is that required to determine the DCS, in the absence of polarization effects, as has been discussed elsewhere.[23,24]

The experimental image, $I_{V/H}(x, y)$, is the outcome of many individual scattering events, and thus the basis image has to be constructed using a great number of trajectories, $i.e.$ it is a sum of many $z(x_n, y_n)$ and $g(\theta_n; \Gamma^n_{V/H})$ functions for individual scattering events,

$$I_{V/H}(x, y) = \sum_n i_{V/H}(x_n, y_n).$$

(11)

The contribution of the different expansion orders can be separated due to the structure of Eq. (9). The summed and convoluted intensity contribution of the l-th order expansion of $\rho^{\{k\}}_{q\pm}(\theta)$ is denoted by $G^{\{k\},V/H}_{q\pm,l}(x, y)$,

$$G^{\{k\},V/H}_{q\pm,l}(x, y) = \sum_n g^{\{k\}}_{q\pm,l}(x_n, y_n, \theta_n; \Gamma^n_{V/H}),$$

(12)

whereas the summed and convoluted apparatus function is referred as $Z(x, y)$

$$Z(x, y) = \sum_n z(x_n, y_n).$$

(13)

Both the sum and the difference of the V and H images can be expressed with the aid of the $G^{\{k\},V/H}_{q\pm,l}(x, y)$ and $Z(x, y)$ functions. Likewise, the basis function for the $(V-H)/(V+H)$ difference image of the l-th order expansion of $\rho^{\{k\}}_{q\pm}(\theta)$, $B^{\{k\}}_{q\pm}(x, y)$, can be constructed from the $G^{\{k\},V/H}_{q\pm,l}(x, y)$ and $Z(x, y)$ functions

$$B^{\{k\}}_{q\pm,l}(x, y) \equiv \frac{G^{\{k\},V}_{q\pm,l}(x, y) - G^{\{k\},H}_{q\pm,l}(x, y)}{2P_{\text{scat}}(\theta) Z(x, y) + \sum_{k,q} \sum_{l=0}^{N^{\{k\}}_{q\pm}} c^{\{k\}}_{q\pm,l} \left[G^{\{k\},V}_{q\pm,l}(x, y) + G^{\{k\},H}_{q\pm,l}(x, y) \right]}.$$

(14)

The whole normalized difference image can be recovered as a sum of the basis set images, as shown below

$$\frac{(V - H)}{(V + H)} \equiv \frac{I_V(x, y) - I_H(x, y)}{I_V(x, y) + I_H(x, y)} = \sum_{k,q} \sum_l^{N^{\{k\}}_{q\pm}} c^{\{k\}}_{q\pm,l} B^{\{k\}}_{q\pm,l}(x, y).$$

(15)

Finally, it should be noted that in addition, each raw basis set image has to be convoluted separately to account for the spatial spread of a single 'hit' on detector, as discussed further in the following subsection.

2. Simulation of the difference images and basis sets

In the following subsection we provide more details of how the experimental difference images are simulated. The same procedures are used to simulate the basis functions, defined in the previous subsection.

The outcome of an 'ideal' scattering experiment can be simulated using the theory outlined in the previous subsection.[23,24] The term ideal refers to the hypothetical situation in which the laser and molecular beams are perfectly aligned in the same plane, the interaction volume is restricted to a certain point, the duration of all the interactions are infinitely short, and the molecular beams are ideally monoenergetic. In other words, every scattering event results in the same scattering (Newton) sphere. The simulated normalized difference images for an ideal scattering experiment are shown in the left column of Fig. 2 for the final states, $|1/2, 8.5, -1\rangle$ and $|3/2, 9.5, +1\rangle$. All the features are sharp and clearly distinguishable.

In reality, the ideal conditions described above cannot be realized in an experiment. The molecular beams have both a spatial and temporal spread. The velocities of the collision partners vary according to a certain finite distribution. Scattered molecules originating from different portions of the beams or from different times will have different detection probabilities. The influence of these effects on the experimental $(V-H)/(V+H)$ image can be accounted for by Monte Carlo modeling, the details of which we have discussed previously in the context of extracting the DCSs from raw velocity-map ion images.[23,24]

For each trajectory the direction and magnitude of the initial velocity of the NO(X) molecule was randomly sampled using the experimental parameters. The temporal coordinate and probability of the interaction between the Ar atom and NO(X) molecule was also calculated. Both laser beams were assumed to have Gaussian spatial intensity profiles, which were used to calculate the probability of the $(1+1')$ REMPI transitions. In this manner, an apparatus function was constructed assuming an isotropic angular distribution of the scattered products. The probability of the $A^2\Sigma \leftarrow X^2\Pi$ transition due to collision induced alignment was taken into account using Eq. (1). Since the electron cloud originating from one ion spreads over a number of pixels of the detector, the apparatus function was also blurred with a Gaussian spatial distribution. The full-width-at-half maximum was 2.5 pixels, which was determined by investigating the individual experimental ion-images. The ideal and full simulated images are compared in Fig. 2 for the $|1/2, 0.5, -1\rangle \rightarrow |1/2, 8.5, -1\rangle$ and

$|1/2, 0.5, -1\rangle \rightarrow |3/2, 9.5, +1\rangle$ transitions. The simulations employ the CC QM renormalized PDDCSs,[6] obtained using the CCSD(T) potentials of Alexander.[8]

Fig. 2 demonstrates that the general features of the ideal simulations are present in the full simulated images. However, the sudden changes in intensity observed in the ideal simulations are somewhat washed out in the full simulation, reflecting the finite angular resolution of the experiment. This is most apparent in the forward scattered region of the simulated image for the $|3/2, 9.5, +1\rangle$ final state. In the forward scattered region, the intensity in the ideal simulation drops rapidly below zero within a range of $5° - 10°$, while in the full simulation it slowly decreases to around zero, and does not take negative values. The above suggests that an accurate modeling of the experimental data requires the use of a full Monte Carlo simulation of the experiment. The same simulation procedures are required to generate accurate basis functions used in the fitting of experimental data, as described in the next subsection.

3. Iterative fitting algorithm in the Fourier space

The objective of the fitting process is to retrieve the renormalized PDDCSs from the experimental images, *i.e.* to ascertain the $c_{q\pm,l}^{\{k\}}$ expansion coefficients given in Eq. (8). One possible way to achieve this is to maximize the overlap of the experimental and the fitted image pixel by pixel by adjusting the expansion coefficients. This method is quite time consuming. Fitting the Fourier moments of the basis set images against those of the experimental image has proven to be a quick and robust alternative.[57] Since the Fourier transform is linear it is possible to factor out the $c_{q\pm,l}^{\{k\}}$ coefficients from the numerator of the basis images. The problem is that the basis functions, $B_{q\pm,l}^{\{k\}}$, are still non-linear in $c_{q\pm,l}^{\{k\}}$, because they appear in the denominator of Eq. (14). This means that each pixel in the basis set has to be re-calculated and the Fourier moments regenerated once any of the expansion coefficients are modified. This complicates and slows down the fitting. This can be overcome by the iterative adjustment of the expansion coefficients outlined below.

As an initial guess, the basis images are generated using the quantum mechanical expansion coefficients. During each subsequent optimization step, the expansion coefficients are varied in the numerator, but kept fixed in the denominator until the error function is minimized. Then the basis images are re-generated with the optimized set of expansion co-

efficients. This procedure is repeated until there is no further decrease in the error function. In this case the Fourier moments of the simulated images have to be generated only prior to each iteration, while the $G_{q\pm,l}^{\{k\}}$ functions have to be generated only once before the first iteration because they are independent of the renormalized PDDCSs. There is no reference to the initial guess after the first iteration. Choosing the QM expansion coefficients to be the initial guess only results in reducing the number of the iterations necessary for convergence of the fits. Within the uncertainties in the measurement (see section III B 4), the outcome of the fit was found not to depend significantly on the initial guess of coefficients, and any arbitrary initial set of PDDCSs converges to near-identical final experimental PDDCSs.

A second difficulty with the basis function fitting method is that formally the basis functions of the difference images, (V−H)/(V+H), depend on the DCS, $P_{\text{scat}}(\theta)$, according to Eqs. (9) and (14). Whilst it would be possible to fit to the raw H and V images to extract simultaneously the DCS and PDDCS data, it turns out that the basis functions are essentially independent of the assumed DCS, and weighting the basis functions by the DCSs is not required. The reason for this is that for a given pixel on the detector, with coordinates (x, y), the DCS is almost constant, because only a small range of scattering angles contribute to a given pixel. For this reason, the DCS terms in the numerator and denominator of Eq. (14) very nearly cancel. This is demonstrated in Fig. 3, which shows simulated images for the spin-orbit conserving transition to $j' = 8.5, f$. The top row of the figure shows three simulated (V−H)/(V+H) difference images, all of which use the QM PDDCS data as input, using either the 'ideal' simulation (described above), a full simulation without a DCS weighting function, and a full simulation in which the DCS is used correctly as a weighting function in determining of the (V−H)/(V+H) difference images and basis functions. Also shown in the second and third rows of the figure are the effects of the different basis functions on the PDDCSs returned by the fitting procedure. Clearly, ignoring the weighting by the DCS when generating the basis functions for the PDDCSs, Eq. (14), is seen to provide an excellent approximation to the correctly weighted functions, and the returned PDDCSs are in excellent agreement with the input QM ones. Even the PDDCSs returned by using the ideal simulated basis functions provide a good qualitative modeling of the input QM data (see the bottom left panels of Fig. 3).

The Legendre polynomials ($P_l(\theta)$) were chosen to serve as the orthonormal bases, (i.e. $W_l(\theta) \equiv P_l(\theta)$) with a maximum expansion order, $N_{q\pm}^{\{k\}} = 6$ (see Eq. (8), and further

discussion in section IV B). In the experimental geometries employed, the contribution of the $\rho_{1+}^{\{2\}}(\theta)$ moment is 2-3 orders of magnitude less than those of the other two $\rho_{q+}^{\{2\}}(\theta)$ terms. For this reason, the basis images for the $\rho_{1+}^{\{2\}}(\theta)$ moment were omitted from the fitting. A genetic algorithm was used to optimize the coefficients.

4. *Error analysis*

In order to estimate the random errors associated with the experimental derived renormalized PDDCSs the following procedure has been adopted. Each normalized difference image consists of approximately 10-12 ion images of 20,000 laser shots. Although an individual difference image is insufficient to determine the renormalized PDDCSs, due to the relatively poor signal-to-noise ratio, triplets or quadruplets of difference images do bear sufficient intensity to retrieve the renormalized PDDCSs. Thus, for each final quantum state studied, the mean values of the $\rho_0^{\{2\}}(\theta)$ and $\rho_{2+}^{\{2\}}(\theta)$ were obtained from fits to these subsets of images, and the standard deviations, σ, were subsequently calculated from the distribution of returned $\rho_0^{\{2\}}(\theta)$ and $\rho_{2+}^{\{2\}}(\theta)$ values.

The alignment data is also subject to systematic errors are these are discussed in detail in section IV C.

IV. RESULTS AND DISCUSSION

A. The experimental difference images

The experimental difference images for a selection of the spin-orbit conserving transitions are shown in Fig. 4, while those for two spin-orbit changing transitions are shown in Fig. 5. In each figure, the experimental difference images are shown in the left column, the fits to the experimental data are shown in the second column, whilst full simulations of the experimental data using the QM PDDCSs as input are shown in the third column. Apart from the inherent noise in the experimental data, the agreement between the QM simulated and experimental images is excellent, based on comparison of the first and third columns of Figs. 4 and 5. Although the experimental difference images are somewhat noisier than the simulated data, the general features observed in the simulations can be readily recognized in the experimental results.

The rightmost column of Figs. 4 and 5 show the sum of the experimental horizontal and vertical ion images. These (V+H) summed images are sensitive primarily to the associated DCSs. Note that the signal-to-noise ratios of the (V−H)/(V+H) images (second column from the right) are poorer in regions where the intensity in the (V+H) summed images is small. Major discrepancies between the experiment and simulation are only observed in regions where the DCS is small. Conversely, the best signal-to-noise ratio and the sharpest features in the difference images are found in the most intense regions of the raw summed (V+H) images.

It has been shown previously for NO(X) + He and Ar that the DCSs belonging to the same parity pair transitions are nearly identical.[20,23] The (V+H) data shown in the 3rd and 4th row of Fig. 4 demonstrate an example of this parity pair relationship for NO(X) + Ar. The present difference images show additional experimental evidence for the same relationship existing for the renormalized PDDCSs. The line strength factor, $h^{(2)}(j_i, j_f)$, is negative for R-branch transitions and unity for Q-branch transitions, and as a result the intensity of the normalized difference image is inverted for the same transition when switching from R- to Q-branch detection. The $|1/2, 7.5, +1\rangle$ image is the negative of the $|1/2, 8.5, -1\rangle$ up to a factor of $h^{(2)}(8.5, 9.5)/(1 - h^{(2)}(8.5, 9.5)) \approx 0.75$ in the 3rd and 4th rows of Fig. 4. These findings imply that the second order renormalized PDDCS are nearly the same for the parity conserving $|1/2, 0.5, -1\rangle \rightarrow |1/2, 7.5, +1, \rangle$ and $|1/2, 0.5, -1\rangle \rightarrow |1/2, 8.5, -1\rangle$ collisions which make up a parity pair.

Qualitative alignment information about $\boldsymbol{j'}$ can be deduced directly from the experimental normalized difference images. If the vertical transition probability is greater than the horizontal, $I_V > I_H$, the intensity is positive. Negative intensity indicates that $I_V < I_H$, whilst a value of zero corresponds to a case when the transition probabilities are roughly the same. Let us consider only the R-branch of the NO $A^2\Sigma^+ \leftarrow X^2\Pi$ electronic transition. In this case the transition dipole moment, $\boldsymbol{\mu}$, lies perpendicular to the molecular axis, and is also perpendicular to $\boldsymbol{j'}$ in the classical high-j limit. The transition probability is the greatest if the electric vector, $\hat{\boldsymbol{\epsilon}}$, of the laser light is aligned parallel to the transition dipole moment, and lowest if it is aligned perpendicular. When detecting on an R-branch, positive intensity, $I_V > I_H$, therefore implies that the transition dipole moment preferentially lies out of the scattering plane. This suggests that $\boldsymbol{j'}$ lies preferentially in the scattering plane, and the scattered NO(X) molecule thus rotates like a 'propeller' or 'cartwheel' depending

14

on the direction of $\boldsymbol{k}'$. In contrast, when $I_V < I_H$, the difference image is negative, and the molecule preferentially rotates like a frisbee, with $\boldsymbol{j}'$ lying perpendicular to the collision plane.

All of the R-branch difference images exhibit decreasing intensity as a function of the scattering angle. The positive intensity, $(I_V > I_H)$, in the forward scattered region is followed by a region where $I_V \approx I_H$. The sideways and backward scattered sections have negative intensity. This means that the molecular rotation is characterized by propeller-like behaviour in the forward scattered region, and smoothly turns into a frisbee-like motion in the backward scattered region, where repulsive forces become dominant. By comparing the difference images, it is noticeable that the extension as well as the average modulus of the positive section of the difference images shrinks as j' increases from $j' = 6.5$, to $j' = 10.5$. On the other hand, the sideways and backward scattered region of the difference images become more negative with increasing j'. Thus, the products departing towards small scattering angles become less aligned with increasing j', whilst those leaving in the opposite direction with respect to the initial relative velocity become more strongly aligned with $\boldsymbol{j}'$ perpendicular to the scattering plane.

B. The fitted difference images

The experimental difference images were used to retrieve the experimental renormalized PDDCSs, as described in section III. The whole scattering angle region was fitted except for the $|1/2, 0.5, -1\rangle \rightarrow |1/2, 7.5, -1\rangle$ transition, where only the $0° - 90°$ portion of the image was taken into account, because of the low scattering intensity outside this region. In general, the fitted images compare very well with the experimental ones, as seen from a comparison of the first and second columns of Figs. 4 and 5. The difference images returned by the fitting procedure are somewhat smoother than the experimental ones, reflecting the noise in the experimental data, and the number of moments used to fit the PDDCS data, and are generally in excellent agreement with those obtained from full QM simulations (the third column in Figs. 4 and 5).

As discussed in section III, the experimentally derived $\rho_{q\pm}^{\{k\}}(\theta)$ renormalized PDDCSs were constructed in terms of Legendre polynomial series expansions (see Eq. (8)), with the $c_{q\pm}^{\{k\}}$ expansion coefficients obtained from the fits to the experimental difference images.

Before presenting the derived PDDCS data, we explore how the returned PDDCSs are influenced by the number of Legendre polynomial moments employed in the fits. The set of basis differences images is more flexible if higher order Legendre polynomials functions are included. The fitted PDDCS are thus expected to approximate the quantum mechanical ones more faithfully by employing an extended set of basis images. All of the experimental images were fitted using a sequence of larger Legendre moment basis set images ranging from $l = 2$ to $l = 9$. The general scattering angle dependence of the QM PDDCS can be recovered even with fits using $l \leq 5$. With up to $l = 5$ Legendre functions, the returned PDDCSs are similar to the theoretical ones. When the number of basis functions employed exceeds $l = 5$, the goodness of fit reaches a plateau, and the experimental PDDCSs exhibit oscillatory structure due to the high number of basis images employed. We therefore decided to choose to truncate the basis set for the $\rho_0^{\{2\}}(\theta)$ parameters at $l = 5$ so that these artifacts are washed out, whilst the polarization information can still be reliably recovered. In general, the experiments are less sensitive to the $\rho_{2+}^{\{2\}}(\theta)$ polarization parameters, and the maximum number of Legendre moments was restricted to $l = 3$.

C.   Lambda-doublet resolved renormalized PDDCSs

The renormalized PDDCSs for the spin-orbit conserving and changing transitions derived from the experimental difference images are shown in Figs. 7 and 8, respectively. The renormalized PDDCS data in each figure are shown along side the CC QM and experimental DCSs (left panels) obtained previously.[23,24] The experimental renormalized PDDCS results are also compared with the results of the CC QM dynamical calculations discussed in detail in the accompanying paper.[6] The agreement between the experimental and CC QM renormalized PDDCS is generally very good for all of the transitions investigated. We emphasize in particular the good agreement between the QM and experimental renormalized PDDCSs for both the spin-orbit conserving and spin-orbit changing transitions. These results provide a particularly demanding test for both the V_{sum} and V_{diff} PESs employed in the CC QM dynamical calculations.[6,8] Although the $\rho_0^{\{2\}}(\theta)$ renormalized PDDCSs compare somewhat better with their QM counterparts than the $\rho_{2+}^{\{2\}}(\theta)$ renormalized PDDCSs, both agree with the QM data within the experimental error limits. It is also worth noting that the deviation between the experimental and quantum mechanical $\rho_0^{\{2\}}(\theta)$ renormalized PDDCS

is somewhat more pronounced for backward scattered products, due to the relatively low signal intensities in this region. Thus the errors in the renormalized PDDCSs are greatest when the DCSs (shown in the left panels of Figs. 7 and 8) are smallest.

Although in general the agreement between experiment and theory is very good, some relatively small discrepancies do remain. For example, as noted above whilst the $\rho_0^{\{2\}}(\theta)$ renormalized PDDCSs agree well with theory in the forward scattered region, discrepancies with theory are observed in the backward scattered region, where the signal is generally weakest for the states investigated. Discrepancies with theory are also more noticeable for the $\rho_{2+}^{\{2\}}(\theta)$ renormalized PDDCSs, as is discussed further below. Systematic errors in the derived alignment parameters can originate from a number of different sources. One such source is the partial saturation of the REMPI signal due to the use of too high a laser intensity for the 226 nm probe radiation. Given that saturation would affect the measured alignment over all scattering angles near equally, contrary to what is observed experimentally, and that great care was taken to avoid saturation using low probe laser intensities, we believe saturation is not the main source of systematic error in our measurements. Another potential source of error is the assumption of full saturation of the ionization step of the REMPI process, and therefore that the $(1+1')$ REMPI process is insensitive to the polarization of the of the 308 nm excimer laser ionizing radiation. We believe this also to be a relatively minor problem, which would again affect the data equally over all scattering angles. Stray magnetic fields, including the earths magnetic field, are another potential source of error. Stray magnetic fields act to depolarize the NO(X) scattered products, and have most effect on those NO(X) molecules which spend the longest time in the scattering center, *i.e.* those with the lowest lab velocities. Although we have taken precautions to mitigate against the effect of stray fields, in particular by placing μ-metal shielding around the scattering region, it is possible that they play some role in the underestimation of the $\rho_0^{\{2\}}(\theta)$ moment in the backward scattered region, where the lab frame velocities of the scattered NO(X) tend to be smaller than for those in the forward scattered region. In this context, it should also be mentioned that hyperfine coupling will also lead to some depolarization of the angular momentum alignment, particularly for the lowest rotational levels studied ($j' = 5.5$ in this case). However, the effect of hyperfine depolarization is relatively small compared with the statistical uncertainties,[58] and would lead to around a 10% reduction in the alignment for the lowest $j' = 5.5$ state investigated here. A final potential source of error arises from

background scattered signal, which mainly affects the forward scattered region of the raw ion images at low Δj. As has been discussed previously, this background arises mainly from inelastic scattering of NO(X) within the hexapole,[23,24] and is relatively unimportant for the states probed here. Therefore, we do not believe it plays a significant role in the systematic errors in the present experiments.

The somewhat poorer quality of the experimentally derived $\rho_{2+}^{\{2\}}(\theta)$ renormalized PDDCSs (right panels of Figs. 7 and 8) compared with the $\rho_0^{\{2\}}(\theta)$ renormalized PDDCSs (middle panels) can be explained as follows. If the experimental conditions were ideal, the Θ and χ angles in Eq. (6) would take fixed values for all of the trajectories, depending only on whether horizontal or vertical polarization was applied. In this hypothetical case, only the azimuthal angle, φ, would vary from pixel to pixel. Based on the comparison of the simulated and experimental images, it is a reasonable assumption that the experimental setup lies quite close to the ideal one. For this reason, the contribution of $\rho_0^{\{2\}}(\theta)$ is nearly constant in a stripe perpendicular to the relative velocity (symmetry) axis of the image. The variation of the total intensity of such a stripe along the symmetry axis is therefore important when extracting the $\rho_0^{\{2\}}(\theta)$ polarization moment. However, the second component of the second order renormalized PDDCS, $\rho_{2+}^{\{2\}}(\theta)$, is multiplied by a factor of $\cos(2\varphi)$. Thus the retrieved value of this moment depends on the intensity distribution within a perpendicular stripe, as well as the variation of the overall intensity along the relative velocity axis. Because the experimental images are slightly asymmetric and have portions of low signal-to-noise, this has a somewhat distorting effect on the retrieved experimental $\rho_{2+}^{\{2\}}(\theta)$ renormalized PDDCSs.

In previous work on the Λ-doublet averaged alignment data, Chandler and coworkers found that the $\rho_0^{\{2\}}(\theta)$ renormalized PDDCSs were consistently less negative than the quantum mechanical ones in the sideways and backwards scattered regions.[44] The Λ-doublet averaged $\rho_{2+}^{\{2\}}(\theta)$ published by Chandler and coworkers[44] are less negative than the present data, revealing less alignment for the forward scattered products, but overall they agree well with the QM results in the backward scattered region. In general, though, the discrepancies between theory and experiment observed in the present fully quantum state resolved work are smaller than those found in the quantum state-averaged results of Chandler and coworkers.

The present PDDCS data confirm the qualitative conclusions about the angular momen-

tum alignment inferred from the intensity distribution of the difference images. The forward scattered products have $\boldsymbol{j'}$ aligned preferentially parallel to $\boldsymbol{k}$ and $\boldsymbol{k'}$, which corresponds to a propeller-like rotational motion.[6] With increasing scattering angle, $\rho_0^{\{2\}}(\theta)$ gradually approaches its lower limiting value of $-\frac{1}{2}$, indicating frisbee-like motion. The backward scattered region is dominated by the repulsive character of the interaction potential. As a general trend, the $\rho_0^{\{2\}}(\theta)$ shift downwards across the entire scattering region as the degree of the rotational excitation increases. This is consistent with the collision becoming more impulsive, and the dynamics responsible for the alignment being governed mainly by classical hard-shell interactions. This is in concordance with our previous theoretical results.[6]

Theoretically, the perfectly forward scattered molecules are not aligned with respect to the x or y axes, *i.e.* $\rho_{2+}^{\{2\}}(\theta = 0) = 0$. This moment then rapidly decreases at small scattering angles. However, the experimental $\rho_{2+}^{\{2\}}(\theta)$ is not zero at $\theta = 0$ for all cases due to the finite experimental resolution. The general trend in $\rho_{2+}^{\{2\}}(\theta)$ follows the QM one and, in turn, coincides with that predicted by the apse model discussed in the accompanying paper.[6] The $\rho_{2+}^{\{2\}}(\theta)$ moment reaches its minimum at small scattering angles then approaches zero when perfectly backwards scattered.

We have shown previously that the experimental and CC QM fully quantum state resolved DCSs are in excellent agreement within the experimental error limits.[23,24] The present study demonstrates that the corresponding experimental and CC QM renormalized $k = 2$ PDDCSs agree almost to the same extent.

D.   Origin of the collision induced alignment

In the accompanying paper,[6] we show that impulsive forces are primarily responsible for the collision induced rotational angular momentum alignment in the NO(X) + Ar system. In particular, we demonstrate that the $k = 2$ CC QM PDDCSs and alignment parameters can be reproduced very well using the kinematic apse model, in which the projection of $\boldsymbol{j}$ along the kinematic apse is conserved. In the context of the present work, in which the initial state is $j = 1/2$, this implies that the projection of $\boldsymbol{j'}$ along the apse direction is restricted to $m_{j'}^a = \pm 1/2$. As j' increases, the apse model therefore predicts that $\boldsymbol{j'}$ becomes increasingly aligned perpendicular to the apse direction. The change in angular momentum alignment with scattering angle, such that $\rho_0^{\{2\}}(\theta)$ is positive in the forward scattered region

and negative for backward scattering, was shown in the accompanying paper to primarily reflect the transformation from the apse frame, where the impulsive alignment is imposed, to the scattering frames, where observations are typically made. Fig. 9 illustrates schematically this impulsive origin of the angular momentum alignment at high-j. As indicated in the figure, appropriate averaging about the dihedral angle in the extreme forward and backward scattered regions means that forward scattered NO(X) preferentially rotate like propellers, while backward scattered NO(X) preferentially rotate like frisbees.

V. CONCLUSIONS

Rotational angular momentum alignment effects in the rotationally inelastic collisions of NO(X) with Ar have been investigated by means of a hexapole state selection, velocity-map ion imaging apparatus at a center-of-mass collision energy of 66 meV. Fully quantum state resolved second order $\rho_0^{\{2\}}(\theta)$ and $\rho_{2+}^{\{2\}}(\theta)$ renormalized polarization dependent differential cross sections have been extracted from the experimental normalized difference (V-H)/(V+H) ion-images using an iterative Fourier moment fitting method. It has been shown that the experimental alignment data, which are presented here for the first time at the fully state-resolved level, are in excellent agreement with the exact quantum mechanical results obtained on the CCSD(T) potential energy surface of Alexander.[8] Combined with the theoretical analysis in the preceding paper,[6] it has been demonstrated experimentally that the hard shell features of the interaction potential mainly govern the rotational alignment of NO(X) induced by collisions with Ar.

REFERENCES

[1]D. A. Case and D. R. Herschbach, Mol. Phys. **30**, 1537 (1975).

[2]D. A. Case, G. M. McClelland, and D. R. Herschbach, Mol. Phys. **35**, 541 (1978).

[3]N. E. Shafer-Ray, A. J. Orr-Ewing, and R. N. Zare, J. Phys. Chem. **99**, 7591 (1995).

[4]F. J. Aoiz, M. Brouard, and P. A. Enriquez, J. Chem. Phys. **105**, 4964 (1996).

[5]M. P. de Miranda, F. J. Aoiz, L. Bañares, and V. S. Rábanos, J. Chem. Phys **111**, 5368 (1999).

[6]M. Brouard, H. Chadwick, C. J. Eyles, B. Hornung, B. Nichols, F. J. Aoiz, P. G. Jambrina, S. Stolte, and M. P. de Miranda, J. Chem. Phys. **xxx**, xxxx (2012).

[7]M. H. Alexander, J. Chem. Phys. **99**, 7725 (1993).

[8]M. H. Alexander, J. Chem. Phys. **111**, 7426 (1999).

[9]M. J. L. de Lange, S. Stolte, C. A. Taajtes, J. Kłos, G. C. Groenenboom, and A. van der Avoird, J. Chem. Phys. **121**, 11691 (2004).

[10]M. J. L. de Lange, M. Drabbels, P. T. Griffiths, J. Bulthuis, S. Stolte, and J. G. Snijders, Chem. Phys. Lett. **313**, 491 (1999).

[11]J. J. van Leuken, J. Bulthuis, S. Stolte, and J. G. Snijders, Chem. Phys. Lett. **260**, 595 (1996).

[12]A. Gijsbertsen, M. J. de Lange, A. E. Wiskerke, H. Linnartz, M. Drabbels, J. Kłos, and S. Stolte, Chem. Phys. **301**, 293 (2004).

[13]P. Andreson, H. Joswig, H. Pauly, and R. Schinke, J. Chem. Phys. **77**, 2204 (1982).

[14]C. R. Bieler, A. Sanov, and H. Reisler, Chem. Phys. Lett. **235**, 175 (1995).

[15]G. C. Corey and M. H. Alexander, J. Chem. Phys. **85**, 5652 (1986).

[16]M. Yang and M. H. Alexander, J. Chem. Phys. **103**, 6973 (1995).

[17]T. Orlikowski and M. H. Alexander, J. Chem. Phys. **79**, 6006 (1983).

[18]J. J. van Leuken, F. H. W. van Amerom, J. Bulthuis, J. G. Snijders, and S. Stolte, J. Phys. Chem. **99**, 15573 (1995).

[19]F. J. Aoiz, J. E. Verdasco, V. J. Herrero, V. S. Rábanos, and M. H. Alexander, J. Chem. Phys. **119**, 5860 (2003).

[20] A. Gijsbertsen, H. Linnartz, A. E. Wiskerke, S. Stolte, D. W. Chandler, and J. Kłos, J. Chem. Phys. **123**, 224305 (2005).

[21] J. Kłos, F. J. Aoiz, J. E. Verdasco, M. Brouard, S. Marinakis, and S. Stolte, J. Chem. Phys. **127**, 031102 (2007).

[22] F. J. Aoiz, J. E. Verdasco, M. Brouard, J. Kłos, S. Marinakis, and S. Stolte, J. Phys. Chem. A **113**, 14636 (2009).

[23] C. J. Eyles, M. Brouard, C.-H. Yang, J. Kłos, F. J. Aoiz, A. Gijsbertsen, A. E. Wiskerke, and S. Stolte, Nature Chemistry **3**, 597 (2011).

[24] C. J. Eyles, M. Brouard, H. Chadwick, B. Hornung, B. Nichols, C.-H. Yang, J. Kłos, F. J. Aoiz, A. Gijsbertsen, A. E. Wiskerke, and S. Stolte, Phys. Chem. Chem. Phys. **14**, 5403 (2012).

[25] C. J. Eyles, M. Brouard, H. Chadwick, F. J. Aoiz, J. Kłos, A. Gijsbertsen, X. Zhang, and S. Stolte, Phys. Chem. Chem. Phys. **14**, 5420 (2012).

[26] A. G. Suits, L. S. Bontuyan, P. L. Houston, and B. J.Whitaker, J. Chem. Phys. **96**, 8618 (1992).

[27] M. S. Eliof and D. W. Chandler, J. Chem. Phys. **117**, 6455 (2002).

[28] M. S. Westley, K. T. Lorenz, D. W. Chandler, and P. L. Houston, J. Chem. Phys. **114**, 2669 (2001).

[29] P. Casavecchia, A. Laganà, and G. G. Volpi, Chem. Phys. Lett. **112**, 445 (1984).

[30] S. D. Jons, J. E. Shirley, M. T. Vonk, C. F. Giese, and W. R. Gentry, J. Chem. Phys. **97**, 7831 (1992).

[31] S. D. Jons., J. E. Shirley, M. T. Vonk, F. Clayton, F. Giese, and W. R. Gentry, J. Chem. Phys. **105**, 5397 (1996).

[32] L. S. Bontuyan, A. G. Suits, P. L. Houston, and B. J. Whitaker, J. Phys. Chem. **97**, 6342 (1993).

[33] H. Kohguchi, T. Suzuki, and M. H. Alexander, Science **294**, 832 (2001).

[34] R. Schinke, Chem. Phys. **34**, 65 (1978).

[35] H. Meyer, J. Chem. Phys. **102**, 3151 (1995).

[36] Y. Kim, H. Meyer, and M. H. Alexander, J. Chem. Phys. **121**, 1339 (2004).

[37] Y. Kim and H. Meyer, Chem. Phys. **301**, 273 (2004).

[38] D. K. Hoffman, J. W. Evans, and D. J. Kouri, J. Chem. Phys. **80**, 144 (1984).

[39] V. Khare, D. J. Kouri, and D. K. Hoffman, J. Chem. Phys. **74**, 2275 (1981).

[40] A. J. McCaffery, M. J. Proctor, and B. J. Whitaker, Annu. Rev. Phys. Chem. **37**, 223 (1986).

[41] K. T. Lorenz, D. W. Chandler, J. W. Barr, W. Chen, G. L. Barnes, and J. L. Cline, Science **293**, 2063 (2001).

[42] P. Jambrina, J. Kłos, F. Aoiz, and M. de Miranda, Phys. Chem. Chem. Phys. **14**, 9826 (2012).

[43] J. L. Cline, K. T. Lorenz, E. A. Wade, J. W. Barr, and D. W. Chandler, J. Chem. Phys **115**, 6277 (2001).

[44] E. A. Wade, K. T. Lorenz, D. W. Chandler, J. W. Barr, and G. L. Barnes, Chem. Phys. **301**, 261 (2004).

[45] See the Supplementary Material at [URL xxxxx] for more information about the polarization parameters used in the present work, and a detail description of the link between the Fano and Macek treatment used here and similar treatments described elsewhere in the literature.

[46] M. G. Tenner, E. W. Kuipers, W. Y. Langhout, A. W. Kleyn, G. Nicolasen, and S. Stolte, Surface Science **236**, 151 (1990).

[47] A. T. J. B. Eppink and D. H. Parker, Rev. Sci. Instrum. **68**, 3477 (1997).

[48] R. Uberna, R. D. Hinchliffe, and J. I. Cline, J. Chem. Phys **105**, 9847 (1996).

[49] HIBRIDON is a package of programs for the time-independent quantum treatment of inelastic collisions and photodissociation written by M. H. Alexander, D. Manolopoulos, H.-J. Werner, and B. Follmeg, with contributions by P. F. Vohralik, D. Lemoine, G. Corey, R. Gordon, B. Johnson, T. Orlikowski, A. Berning, A. Degli-Esposti, C. Rist, P. Dagdigian, B. Pouilly, G. van der Sanden, M. Yang, F. de Weerd, S. Gregurick, and J. Kłos.

[50] D. E. Manolopoulos, J. Chem. Phys. **85**, 6425 (1986).

[51] M. H. Alexander and D. E. Manolopoulos, J. Chem. Phys. **86**, 2044 (1987).

[52] J. Z. H. Zhang and W. H. Miller, J. Chem. Phys. **91**, 1528 (1989).

[53] J. Aldegunde, M. P. de Miranda, J. M. Haigh, B. K. Kendrick, V. Sez-Rbanos, and F. J. Aoiz, J. Phys. Chem. A **109**, 6200 (2005).

[54] U. Fano and J. H. Macek, Rev. Mod. Phys. **45**, 553 (1973).

[55] C. H. Greene and R. N. Zare, Ann. Rev. Phys. Chem. **33**, 119 (1982).

[56] I. V. Hertel and W. Stoll, Adv. At. Mol. Phys. **13**, 113 (1977).

[57] M. J. Bass, M. Brouard, A. P. Clark, and C. Vallance, J. Chem. Phys. **117**, 8723 (2001).

[58]M. Rutkowski and H. Zacharias, Chem. Phys. **301**, 189 (2004).

[59]A. J. Orr-Ewing and R. N. Zare, Ann. Rev. of Phys. Chem. **45**, 315 (1994).

Macek and Fano[54]	Orr-Ewing[59]	Hertel-Stoll[56]	de Miranda[5]	de Miranda[5] *
real	*real*	*real*	*complex*	*real*
O_0	$c_1(j)\mathcal{A}_0^{\{1\}}$	$c_1(j)A_0^{\{1\}}$	$c_1(j)a_0^{(1)}$	$c_1(j)a_0^{\{1\}}$
A_0	$\mathcal{A}_0^{\{2\}}$	$A_0^{\{2\}}$	$c_2(j)a_0^{(2)}$	$c_2(j)a_0^{\{2\}}$
A_{1+}	$\frac{1}{\sqrt{3}}\mathcal{A}_{1+}^{\{2\}}$	$\frac{1}{\sqrt{3}}A_{1+}^{\{2\}}$	$\frac{2}{\sqrt{6}}c_2(j)a_{\pm1}^{(2)}$	$\frac{1}{\sqrt{3}}c_2(j)a_{1+}^{\{2\}}$
A_{2+}	$\frac{1}{\sqrt{3}}\mathcal{A}_{2+}^{\{2\}}$	$\frac{1}{\sqrt{3}}A_{2+}^{\{2\}}$	$\frac{2}{\sqrt{6}}c_2(j)a_{\pm2}^{(2)}$	$\frac{1}{\sqrt{3}}c_2(j)a_{2+}^{\{2\}}$

$$c_1(j) = [j(j+1)]^{-1/2}, \quad c_2(j) = [(2j+3)(2j-1)/(j(j+1))]^{1/2} \ .$$

TABLE I. The relationship between the polarization moments and alignment parameters used in the present work and elsewhere.

*In the case of the differential polarization moments, dependent on the scattering angle θ, the $a_{q\pm}^{\{k\}}$ parameters in this column should be replaced by the renormalized PDDCS, $\rho_{q\pm}^{\{k\}}(\theta)$, used in this work.

FIG. 1. Left panel: A schematic diagram of the experimental arrangement of the laser and molecular beams. The NO(X) and the Ar beams intersect each other at right angles. In the present experiments, the arrangement is such that the propagation axis of the probe laser, k_p, is nearly perpendicular to the relative velocity of the colliding partners, k, and is coplanar with the molecular beams. The excimer laser propagates in the same plane. The probe geometries 'V' and 'H' refer to the probe laser polarization vector lying either parallel to the time-of-flight axis, or in the plane of the molecular beams, almost parallel with k, as indicated. Middle and right panels: The angles which relate the detector and scattering frames. The Euler angle χ defines the direction of linear polarization of the light employed (see text for details).

FIG. 2. Comparison of the 'ideal' and 'full' simulated difference (V−H)/(V+H) ion images for the transition from the initial state $|\Omega, j, \epsilon\rangle = |1/2, 0.5, -1\rangle$ to the two final states indicated. The transitions employed are given in section II. Positive intensity is shown as yellow/red, negative intensity as blue. See text for details. In this and subsequent figures, forward scattering corresponds to the top left of the images, as indicated by the arrow shown in the top left panel.

FIG. 3. Top row: Simulations of the difference (V−H)/(V+H) ion images for the $\Delta j = 8$ spin-orbit and parity conserving transition from the initial state $|1/2, 0.5, -1\rangle$. The simulations employ the CC QM PDDCS data. The figure shows the results of the 'ideal' simulation (left column) and the full simulation (middle column), both obtained without appropriate weighting by the DCS. The right hand column shows the results of a full simulation, this time including the weighting by DCS in the basis function generation. Second and third row: the $\rho_0^{\{2\}}(\theta)$ and $\rho_{2+}^{\{2\}}(\theta)$ renormalized PDDCSs returned by fitting the full simulated images with the basis sets generated as indicated in the three columns. See text for details.

FIG. 4. Comparison of the difference $(V-H)/(V+H)$ ion-images derived experimentally (left column), returned from the fits to the experimental data (second column), and from the full simulation using the CC QM data (third column) for the spin-orbit conserving transitions from $|1/2, 0.5, -1\rangle$ to the states shown. The color scheme for the collision induced alignment data is identical with that of Fig. 2. The difference images are mainly sensitive to the rotational alignment and the PDDCSs. The right column shows the corresponding experimental summed $(V+H)$ ion-images, which are mainly sensitive to the DCSs. Note that the $\epsilon' = -1$ states where probed using the R_{21}-branch lines, while the $\epsilon' = +1$ states were probed on the overlapping $Q_{21}+R_{11}$-branch lines.

FIG. 5. As for Fig. 4, but comparing the difference $(V-H)/(V+H)$ ion-images derived experimentally (left column), returned from the fits to the experimental data (second column), and from the full simulation using the CC QM data (third column) for the spin-orbit changing transitions from $|1/2, 0.5, -1\rangle$ to the states shown. The right column shows the corresponding experimental summed $(V+H)$ ion-images, which are mainly sensitive to the DCSs. Note that these images were obtained using the overlapping $Q_{22}+R_{12}$-branch lines. The color scheme for the collision induced alignment data is identical with that of Fig. 2.

FIG. 6. Comparison of the CC QM and experimental $\rho_0^{\{2\}}(\theta)$ (upper left panel) and $\rho_{2+}^{\{2\}}(\theta)$ (upper right panel) renormalized PDDCS obtained with basis functions of increasing maximum order (l) for the $|1/2, 0.5, -1\rangle \rightarrow |3/2, 5.5, +1\rangle$ transition. The experimental image (middle left panel), and the corresponding fitted ion-images for the different combinations of maximum l value indicated. The color scheme is identical with that of Fig. 2.

FIG. 7. Comparison of the experimental (red dashed line) and CC QM (black solid line) $\rho_0^{\{2\}}(\theta)$ (middle column) and $\rho_{2+}^{\{2\}}(\theta)$ (right column) renormalized PDDCSs for the spin-orbit conserving transitions from $|1/2, 0.5, -1\rangle$ to the states shown. The error bars represent $2\,\sigma$. The left column shows the DCS data obtained from the experiment (red dashed line) and from the CC QM (black solid line) calculations, as presented previously.[23,24] Note that the DCSs show most intensity in the forward hemisphere, and hence the PDDCSs are determined most reliably in this region.

FIG. 8. Comparison of the experimental (red dashed line), CC QM (black solid line) $\rho_0^{\{2\}}(\theta)$ (middle column) and $\rho_{2+}^{\{2\}}(\theta)$ (right column) renormalized PDDCSs for the spin-orbit changing transitions from $|1/2, 0.5, -1\rangle$ to the $|\Omega', j', \epsilon'\rangle$ states shown. The error bars represent $2\,\sigma$. The left column shows the DCS data obtained from the experiment (red dashed line) and from the CC QM (black solid line) calculations, as presented previously.[23,24] Note that the PDDCSs are determined most precisely in the region in which the DCSs are most intense.

FIG. 9. Schematic diagram of the origin of the collision induced angular momentum alignment. Note that close to the forward and backward directions both in-plane and out-of-plane scattering contribute to a given pixel, and the azimuthal angle, ϕ, must be averaged over, as indicated by the black dashed circles.

MCPs

v_{NO}

k

v_{Ar}

k_{308}

V

H

$k_p = k_{226}$

Detector frame

ζ

k_p

k

$-\Theta$

ε

Φ

η

ξ

Scattering frame

z

k

k_p

k'

θ

Θ

φ

x

y

	Ideal simulation	Full simulation	
1/2, 8.5, −1			+0.6
3/2, 9.5, +1			−0.6
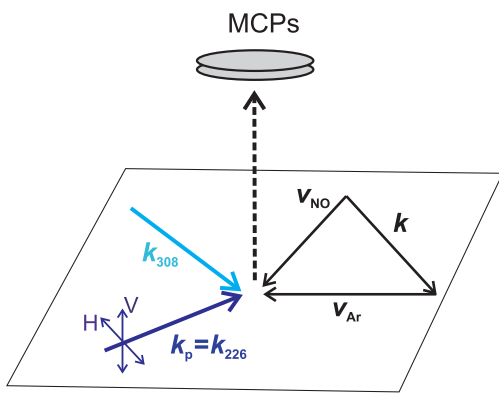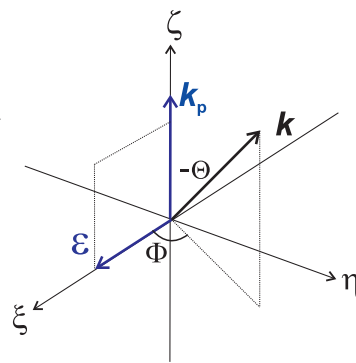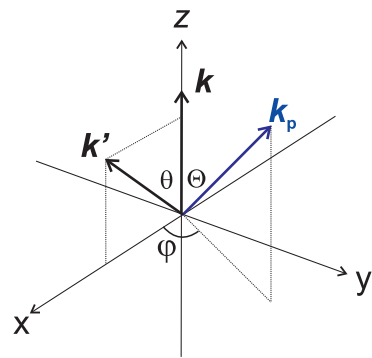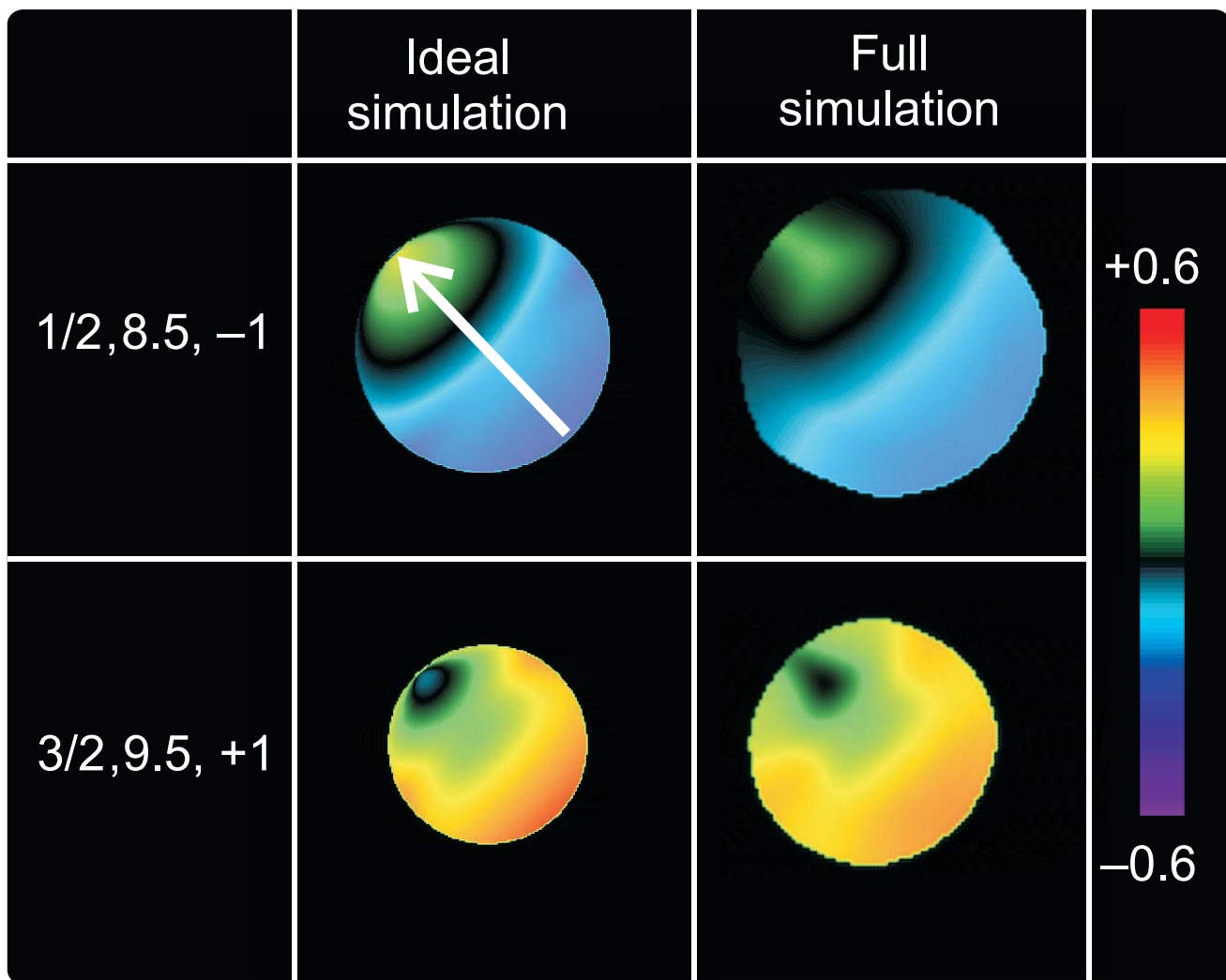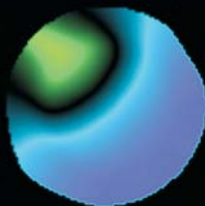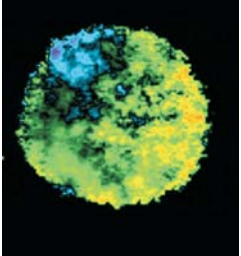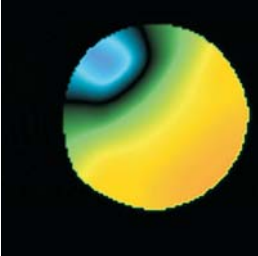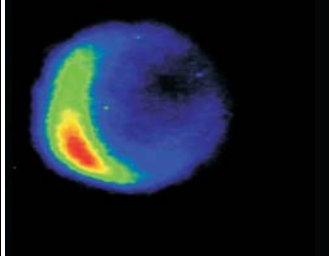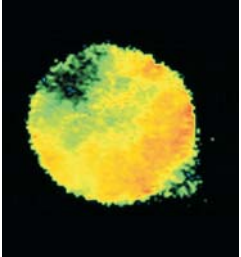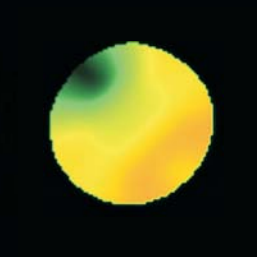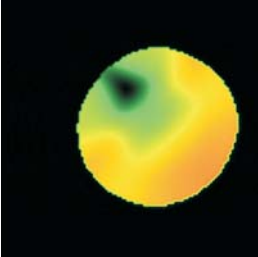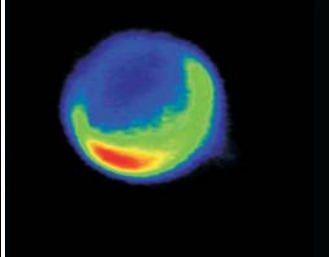
Ideal   Unweighted   Weighted

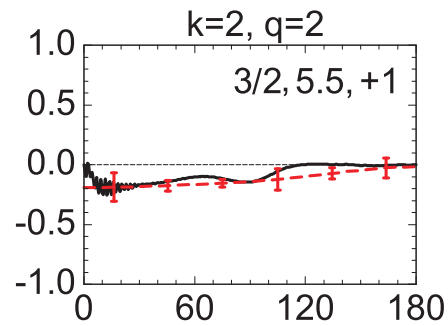|	(V–H)/(V+H) experimental	Fit	(V–H)/(V+H) simulated	V+H experimental
1/2, 6.5, –1				
1/2 , 7.5, –1				
1/2 , 7.5, +1				
1/2, 8.5, –1				
1/2,10.5, -1				

	(V−H)/(V+H) experimental	Fit	(V−H)/(V+H) simulated	V+H experimental
3/2, 5.5, +1				
3/2, 9.5, +1				

$k=2, q=0$

$k=2, q=2$

$\rho^{(k)}_{q+}$

3/2, 5.5, +1

3/2, 5.5, +1

— $l=3$
-- $l=5$
-·- $l=7$
— QM

— $l=2$ -- $l=3$
-·- $l=5$ — QM

θ / degrees

θ / degrees

Experimental

$l_{20}=3$, $l_{22+}=2$

$l_{20}=5$, $l_{22+}=3$

$l_{20}=7$, $l_{22+}=5$

Top column headers: k=2, q=0 (middle column), k=2, q=2 (right column)

Panels labeled (left to right, top to bottom):
1/2, 6.5, −1
1/2, 7.5, −1
1/2, 7.5, +1
1/2, 8.5, −1
1/2, 10.5, −1

Left column y-axis: $(\mathrm{d}\sigma/\mathrm{d}\omega)\,/\,\text{Å}^2$
Middle and right column y-axis: $\rho^{\{k\}}_{q+}$
x-axis: $\theta\,/\,\text{degrees}$

Forward

Backward